Evidence for the Amphipathic Nature and Tilted Topology of Helices 4 and 5 in the Closed State of the Colicin E1 Channel[†]

Derek Ho and A. Rod Merrill*

Department of Molecular and Cellular Biology, University of Guelph, Guelph, Ontario N1G 2W1, Canada

Received October 10, 2008; Revised Manuscript Received December 5, 2008

ABSTRACT: The membrane-bound closed channel structure of helices 4 and 5 (Lys-406−Asp-446) of the colicin E1 channel domain was investigated by using a site-directed fluorescence labeling technique. A bimane probe was covalently attached to a cysteine residue in a series of single-cysteine mutant proteins to scan each helix in a residue-by-residue fashion. A variety of fluorescence properties of the bimane fluorophore were measured for both the soluble and membrane-bound states of the channel peptide, including the fluorescence emission maximum, fluorescence anisotropy, and membrane bilayer penetration depth. The fluorescence properties were collated for construction of a membrane-bound topology model of helices 4 and 5 of the channel domain. Finally, the data reveal that both helices 4 and 5 are two separate amphipathic α-helices that are situated parallel to the membrane surface. Dual fluorescence quencher analysis shows that helix 4 adopts a tilted topology in which its C-terminus is more buried than its N-terminus within the bilayer. In contrast, helix 5 is relatively solvent-exposed and located parallel to the interfacial region of the membrane surface. However, the loop region of both helices 4 and 5 was shown to be relatively buried within the bilayer. In addition, a least-squares fit of the data to a harmonic wave function indicated that both periodicity and frequency are typical for an amphipathic α-helix (3.75 ± 0.1 residues per turn for helix 4 and 3.70 ± 0.1 residues per turn for helix 5). Squared residual plots of the harmonic wave function also reveal that the N-terminus of helix 4 is elongated by two residues from Lys-406 to Phe-404, while the C-terminus of helix 5 is elongated by three residues from Tyr-434 to Ile-437 upon membrane association.

Colicins are antimicrobial proteins produced by *Escherichia coli* which target susceptible bacteria in response to stressful conditions, including nutrient depletion, DNA damage, overcrowding, and anaerobiosis (*1*). Colicins can be grouped into three major categories based on their routes of lethal action: (i) the formation of a depolarizing ion channel in the cytoplasmic membrane, (ii) the inhibition of protein and peptidoglycan synthesis, and (iii) the degradation of nucleic acids (*2*). Because of their ability to invade related Gram-negative bacteria, colicins have become a model for studying bacterial protein import (*3*), protein folding and unfolding (*4, 5*), membrane insertion (*6, 7*), and pore formation (*8*). The protein of interest in this study is colicin E1, which is a member of the ion channel-forming group of colicins; this group also includes colicin A, B, Ia, Ib, K, and N (*9, 10*).

Colicins can be functionally divided as follows: receptor binding, translocation, and catalytic/channel domains (*11*). In the case of colicin E1, it is the catalytic/channel domain that forms the depolarizing ion channel causing target cell death (*12*). For colicin E1 to enter a target bacterium, the receptor-binding domain must first bind to the BtuB outer membrane receptor (vitamin B_{12} receptor) (*13*). The binding of the BtuB receptor induces unfolding of the translocation domain which initiates translocation of the entire protein through the TolC channel and facilitates entry into the periplasm. This translocation process is also mediated by both the TolA and TolQ inner membrane proteins. Finally, the channel domain adopts an insertion-competent conformation in which it spontaneously inserts into the inner membrane to form the closed channel (*14*). The channel then opens in the presence of a trans-negative membrane potential that allows the escape of various ions from the host cells, such as Na^+, K^+, and H^+, and subsequently, cell death ensues (*15*).

A crystal structure of the soluble channel domain has been determined to a resolution of 2.5 Å (*16, 17*). The crystal structure is comprised of 10 separate α-helices that form an extremely stable, water-soluble globular protein. The channel domain is a helical sandwich that is folded into three separate layers: layer A, the outer layer composed of helices 1, 2, and 10; layer B, the inner core layer including helices 5, 8, and 9; and layer C, an outer layer composed of helices 3, 4, 6, and 7 (*11*). Interestingly, this protein also consists of a hydrophobic α-helical hairpin, helices 8 and 9, which acts as the nonpolar core of the protein. These two helices are critical to colicin pore formation as they create a membrane-spanning hairpin upon bilayer association (*4, 11, 18, 19*). Previous fluorescence studies suggested that upon translocation across the host cell outer membrane, colicin adopts an insertion-competent state, which allows the hydrophobic core (helices 8 and 9) to penetrate the target membrane. Thus,

[†] This work was supported by a grant from the Natural Science and Engineering Research Council of Canada (to A.R.M.).

* To whom correspondence should be addressed: Department of Molecular and Cellular Biology, University of Guelph, Guelph, ON, Canada N1G 2W1. Telephone: (519) 824-4120, ext. 53806. Fax: (519) 837-1802. E-mail: rmerrill@uoguelph.ca.

10.1021/bi801906v CCC: $40.75
Published on Web 01/21/2009

the protein unfolds, binds, and spontaneously inserts into the membrane to form the closed channel in a series of kinetically defined steps (*20*). Subsequently, the channel opens in the presence of a trans-negative membrane potential, and the two channel states exist in rapid equilibrium (*21*).

Two well-known structural models have been proposed for the closed channel state, which are the penknife and umbrella models (*22*). The penknife model was based on disulfide bond engineering experiments which suggested that helices 1 and 2 pull away from the body of the protein, with the remaining helices being deeply buried in the lipid bilayer (*22*). In contrast, the umbrella model suggests that only hydrophobic helices, 8 and 9, are inserted into the hydrophobic milieu of the membrane, whereas the eight remaining helices spread out onto the membrane surface to form an umbrella-like structure. In fact, the umbrella model was strongly supported by time-resolved fluorescence resonance energy transfer (FRET) studies on colicin E1 (*23*). However, the exact orientation of the helices, their depth of bilayer penetration, and the details of the lipid and protein contacts still remain unknown. Therefore, the objective of this study was to determine the two-dimensional orientation of each helix relative to the lipid membrane in the closed channel. Recently, we reported on the membrane topology of amphipathic α-helices 1, 2, and 3 of colicin E1 in its closed channel state, and we found that all three N-terminal helices retain their α-helical structure with helix 3 being elongated upon membrane association (*24*−*26*).

Herein, we continue our investigation of the membrane-bound topology of the remaining helices within the closed state of the colicin E1 channel domain with a study of the membrane-bound disposition of helices 4 and 5 (Lys-406−Asp-446). Using site-directed fluorescence labeling combined with our novel helical periodicity analysis method, we found that both helices 4 and 5 are two separate amphipathic α-helices in the membrane-bound closed channel state, in contrast to a previous report (*27*). Additionally, upon bilayer association, the N-terminus of helix 4 is elongated from Lys-406 to Phe-404 while the C-terminus of helix 5 is elongated from Tyr-434 to Ile-437.

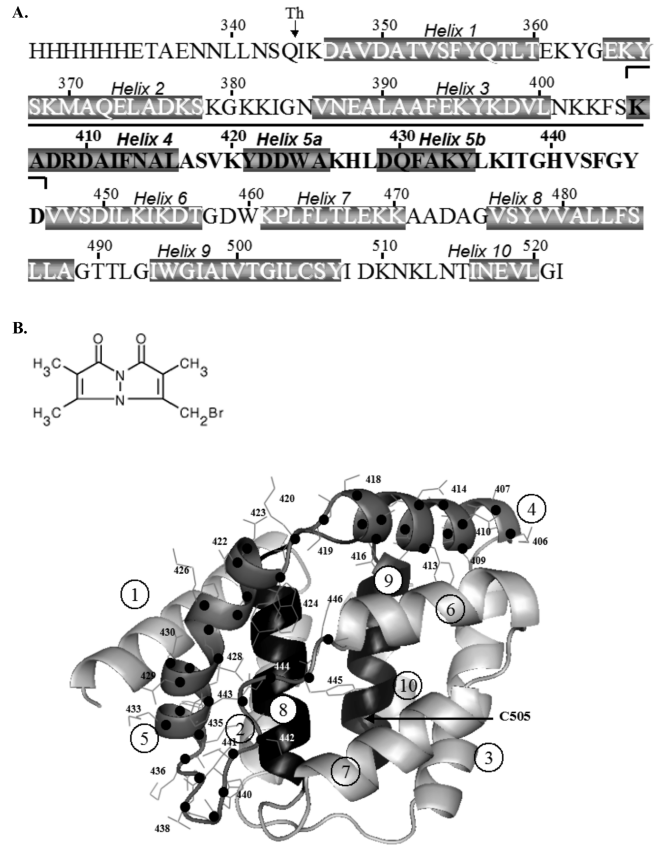

FIGURE 1: Schematic representation of the colicin E1 channel domain. (A) Primary sequence and secondary structure of the channel-forming domain of colicin E1 ($P190H_6$). Residues that are shown in bold and highlighted with a downward-facing brace were subjected to Cys substitutions. The thermolytic digestion site of the channel-forming domain is shown as *Th*. (B) Structure of monobromobimane and ribbon topology diagram of the 2.5 Å crystal structure of the P190 peptide (PDB entry 2I88). The overall structure consists of 10 α-helices, where helices 8 and 9 (colored black) are the hydrophobic helices that serve as a membrane-anchoring helical hairpin in the membrane-associated state. The locations of the cysteine replacements are indicated by both the dark spheres and residue numbers, whereas helices 4 and 5 are highlighted in gray and displayed in both the ribbon and side chain stick format.

EXPERIMENTAL PROCEDURES

Materials. All chemicals, unless otherwise stated, were purchased from Sigma (Oakville, ON). All steady-state fluorescence measurements were conducted with a PTI-Alphascan-2 spectrofluorimeter (Photon Technologies Inc., South Brunswick, NJ) equipped with a thermostated cell holder, and data are reported as the mean ± standard deviation and were recorded in at least triplicate.

Mutagenesis, Protein Purification, and Monobromobimane Labeling. Each residue from Lys-406 to Asp-446 of $P190H_6$[1] was individually replaced with a cysteine using the Stratagene (La Jolla, CA) Quikchange mutagenesis kit. Plasmid DNA was purified using the High Pure Plasmid isolation kit from Roche Diagnostics (Laval, QC). Both the wild-type (WT) $P190H_6$ and Cys mutant proteins were prepared from transformed lexA$^-$ *Escherichia coli* IT3661 cells as described previously (*10*). Protein purities were assessed by SDS−PAGE, and protein concentrations were determined by spectroscopy at A_{280}, using an extinction coefficient (ε) of 29910 M^{-1} cm^{-1} (ε = 24410 M^{-1} cm^{-1} for the Trp mutant protein, W424C, and ε = 28420 M^{-1} cm^{-1} for the Tyr mutant proteins, Y421C, Y434C, and Y445C) (*28*). Purified Cys mutant proteins were labeled with the small fluorophore monobromobimane (mBBr, 271.11 g/mol, Figure 1B) (Molecular Probes, Eugene, OR) at a 20:1 molar ratio (probe:protein), and the labeling efficiency was determined as previously described (*24*).

Preparation of Large Unilamellar Vesicles (LUVs). LUVs were prepared from 1,2-dioleoyl-*sn*-glycero-3-phosphocholine and 1,2-dioleoyl-*sn*-glyerco-3-[phospho-*rac*-(1-glycerol)] vesicles at a 60:40 molar ratio (Avanti Polar Lipids, Alabaster, AL). Lipids were prepared and quantified as

[1] Abbreviations: bimane-Cys, bimane-labeled *N*-acetylcysteine; CSM, cysteine-scanning mutagenesis; $P190H_6$, colicin E1 190-residue channel domain with an N-terminal six-histidine tag; DMG, dimethylglutaric acid; DTT, dithiothreitol; DOPC, 1,2-dioleoyl-*sn*-glycero-3-phosphocholine; DOPG, 1,2-dioleoyl-*sn*-glycero-3-[phospho-*rac*-(1-glycerol)]; HPSA, helix periodicity statistical analysis; LUVs, large unilamellar vesicles; mBBr, monobromobimane; PBS, phosphate-buffered saline; $\lambda_{em,max}$, fluorescence wavelength emission maximum; PDB, Protein Data Bank; Q-ratio, ratio of quenching by KI to that by 10-DN; rpt, residues per turn; SASA, solvent-accessible surface area; SPQ, 6-methoxy-*N*-(3-sulfopropyl)quinolinium; WT, wild-type.

described previously (*24*), except the buffer used to resuspend vesicles consisted of 10 mM DMG and 100 mM NaCl (pH 4.0). Asolectin (Fluka, Oakville, ON) was purified according to the method of Schendel and Reid (*29*), and vesicles were prepared as described previously (*30*). The phospholipid concentration was determined using the microBartlett assay (*24*).

Steady-State Intrinsic Trp Fluorescence. The folded integrity of all proteins was examined using intrinsic Trp fluorescence as previously described (*24*). Both the unlabeled and bimane-labeled mutants as well as WT P190H$_6$ were diluted to 4 μM in PBS [50 mM NaH_2PO_4, 50 mM Na_2HPO_4, and 100 mM NaCl (pH 7.0)]. Intrinsic fluorescence was generated by excitation of Trp residues at 295 nm (2 nm excitation slit width), and emission was detected from 305 to 450 nm (4 nm slit width). The resulting traces were corrected for the buffer and wavelength-dependent bias of the emission components of the spectrofluorimeter before calculation of the λ emission maximum ($\lambda_{em,max}$) from the first derivative of the smoothed spectra.

6-Methoxy-N-(3-sulfopropyl)quinolinium Assay for in Vitro Channel Activity. The 6-methoxy-*N*-(3-sulfopropyl)quinolinium assay was performed as previously described (*30*) using a Cary Eclipse spectrofluorimeter (Varian Instruments, Mississauga, ON). Both the labeled and unlabeled proteins were diluted to 4 μg/mL in extravesicular buffer consisting of 100 mM KCl and 10 mM DMG, and all buffers were adjusted to pH 5.0.

Bimane Fluorescence Emission Spectra. The steady-state bimane fluorescence emission spectra of all Cys mutant proteins were measured as previously described (*24*). All bimane-labeled mutant proteins were diluted to 4 μM in DMG buffer [20 mM DMG and 130 mM NaCl (pH 4.0)] in the presence or absence of excess LUVs (800 μM, final concentration). The data were corrected for the buffer and wavelength-dependent bias of the equipment (*31*) before calculation of the $\lambda_{em,max}$ from the first derivative of the smoothed spectra.

Solvent-Accessible Surface Area (SASA). The SASA of each residue side chain for helices 4 and 5 was determined using GETAREA 1.1 (*26*) with a 1.4 Å water probe after input of the crystal structure coordinates of P190H$_6$ (PDB entry 2I88) (*11*). The data were compared against the bimane fluorescence parameters to probe the local environment of each residue side chain.

Steady-State Bimane Fluorescence Anisotropy. The steady-state fluorescence anisotropy (r) measurements were taken using "T-format" detection by simultaneously comparing the intensities of the vertically (I_{VV}) and horizontally (I_{VH}) polarized emitted light as previously described (*24*). Using the I_{VV} and I_{VH} fluorescence intensities, the anisotropy (r) was calculated as

$$r = \frac{I_{VV} - GI_{VH}}{I_{VV} + 2GI_{VH}} \quad (1)$$

The G instrumental factor, measured as I_{HV}/I_{HH}, was determined from the intensities of the vertically (I_{HV}) and horizontally (I_{HH}) polarized emitted light from horizontally polarized excitation light. All bimane-labeled mutant proteins were diluted to 8 μM in DMG buffer [20 mM DMG and 130 mM NaCl (pH 4.0)] in the presence or absence of excess LUVs (800 μM, final concentration). The excitation wavelength was set at 381 nm (4 nm slit width), and emission was collected at 470 nm (10 nm slit width) with a signal integration time of 30 s. A solvent blank (DMG buffer or LUVs in DMG buffer) was subtracted from each intensity reading prior to the calculation of the anisotropy value. Probe mobility values were determined on the basis of the inverse of the measured anisotropy values.

Dual Quenching Analysis. The depth measurement of each bimane-labeled residue relative to the bilayer was determined by assessing the quenching of bimane using both iodide (KI) and 10-doxylnonadecane (10-DN) as described previously (*32*). To measure iodide quenching (F_{KI}), the sample fluorescence was measured in ratio mode using semimicro quartz cuvettes (0.5 cm × 0.5 cm) containing 100 μM LUVs and 7.5 μg of protein or LUVs only (background). F_{KI} was determined after the addition of a 50 μL aliquot of an aqueous 1.7 M KI solution from a 0.85 mM $Na_2S_2O_3$ stock solution. To measure 10-doxyl-nonadecane (10-DN) quenching, LUVs were prepared as described above except that the LUVs were doped with 10 mol % 10-DN. All the samples were incubated at 24 °C for 30 min before the measurement of initial fluorescence. For all measurements, the excitation wavelength was set at 375 nm with the emission intensity observed at 467 nm (2.5 and 5 nm for both excitation and emission bandpasses, respectively).

Calculation of the Iodide to 10-DN Quenching Ratio (Q-Ratio). The ratio of quenching by 10-DN relative to that by KI (Q-ratio) was used to determine the penetration depth of bimane in lipid bilayers as described previously (*26*). The Q-ratio was calculated from the formula

$$\text{Q-ratio} = \frac{F_0/F_{10\text{-DN}} - 1}{F_0/F_{KI} - 1} \quad (2)$$

where F_0 is the fluorescence of the sample lacking quencher. F_{KI} and $F_{10\text{-DN}}$ are the fluorescence intensities in the presence of KI and 10-DN, respectively.

Prediction of Secondary Structure from Fluorescence Parameters. The secondary structure elements were predicted from the observed fluorescence parameters using a method adopted from Cornette *et al.* (*26, 33*). In brief, the periodicity and the frequency of the observed fluorescence parameters were obtained through a least-squares fitting approach using the harmonic wave function

$$y = a \sin\left[2\pi\left(\frac{x+b}{p}\right)\right] + c \quad (3)$$

where a is the amplitude, b is the phase, p is the period, and c is an offset value. All calculations were made using an Excel 2002 template spreadsheet developed by U. Oehler. The estimates of a, b, c, and p were initially obtained using four different methods of nonlinear least-squares fitting in Statistical Analysis System (SAS) version 9.1 (SAS Institute, Cary, NC). The power spectra of the measured bimane fluorescence $\lambda_{em,max}$ were calculated using the method developed by Cornette and colleagues (*33*).

RESULTS

Mutagenesis, Protein Purification, and mBBr Labeling. The sequence of the colicin E1 channel domain comprising helices 4 and 5 and including residues Lys-406−Asp-446 (Figure 1A) was subjected to cysteine scanning mutagenesis

(CSM), and mutation sites were confirmed with DNA sequencing. In Figure 1B, the spatial relationship of helices 4 and 5 relative to the entire channel peptide is shown. There is only one natural Cys residue (Cys-505) deeply buried within the hydrophobic core of the protein, and under nondenaturing conditions, it does not react with thiol-specific reagents.

All single-Cys proteins exhibited wild-type expression levels except for A432C and H440C, which showed almost no expression. As a result, these two mutants were eliminated from the study. Six of the 15 helix 4 single-Cys mutant proteins were insoluble when expressed as the recombinant $P190H_6$ protein, and these included D408C, D410C, F413C, L416C, A417C, and K420C. In contrast, none of the helix 5 Cys mutant proteins encountered any solubility issues. To overcome the solubility issues for these mutant proteins, the full-length colicin was expressed and followed with thermolysin digestion to isolate the channel domain for this study (*34*). Remarkably, five of the six helix 4 mutants were purified successfully with good yields, and only the full-length D408C had expression problems and was not studied further. Lastly, the purity of all mutant proteins was assessed by SDS−PAGE analysis.

To report on the local environment of the residues within helices 4 and 5, each single-Cys protein was subjected to monobromobimane (mBBr) labeling. The mBBr labeling efficiency, which represents the fraction of the mutant protein being labeled (no label, 0%; complete labeling, 100%) is shown in Figure 2A. Labeling efficiency of most mutants ranged between 50 and 100%, except for a few that showed slightly elevated labeling efficiencies. W424C showed a labeling efficiency of 123%, which suggested that either there is excess mBBr dye trapped within the hydrophobic core of the channel domain or nonspecific labeling at residues other than Cys occurred. Mass spectrometry analysis revealed that the excess labeling efficiency was not due to nonspecific labeling (data not shown). Therefore, it was concluded that excess bimane becomes trapped within the hydrophobic core or adheres to a nonpolar patch on the protein. In addition, small amounts of protein impurity could also contribute to the higher (>100%) labeling efficiencies.

Structural and Functional Analysis of Cys Mutants. To assess the structural integrity of the single-Cys mutants, the Trp fluorescence emission maximum values (Trp $\lambda_{em,max}$) were used. The objective of this measurement is to use the emission wavelength maximum values that originate from the three naturally occurring Trp residues, which can provide a measure of the average local environment of these residues and, hence, the folded integrity of the proteins. Mutation-induced alterations in the folded integrity would be expected to cause a red shift in the Trp $\lambda_{em,max}$ values. As shown in Table 1, the wild type exhibited a Trp $\lambda_{em,max}$ value near 324 nm.

Data from Table 1 suggested that the Trp $\lambda_{em,max}$ values of most single-Cys mutants were similar to that of the WT protein. A few mutants exhibited emission values near 330 nm, which may reflect a small degree of loosening of the hydrophobic core of the channel proteins caused by the mutations. However, results from circular dichroism analysis (CD) of the various mutant proteins confirmed that these mutants possess α-helical content similar to that of the WT protein (data not shown). According to the crystal structure, these mutation sites involve all hydrophobic residues with side chains facing the interior of the protein. It is likely that these residues provide critical noncovalent interactions with neighboring residues that help to shape the globin-like fold of the channel protein. Furthermore, the Trp $\lambda_{em,max}$ data support the idea that the relatively small size of the mBBr fluorophore causes little structural perturbation of the channel protein.

To demonstrate that both the Cys replacement and the bimane attachment did not significantly affect the channel activity, the SPQ [6-methoxy-*N*-(3-sulfopropyl)quinolinium] activity assay was performed to measure the *in vitro* channel activity of the protein (*24*−*26*). As shown in Table 1, most Cys mutants (nonlabeled) exhibited channel activities ranging from 84 to 125% of the WT level, which supported the Trp emission and CD data that Cys substitution did not alter the folded integrity of the channel proteins. Furthermore, to assess whether bimane attachment caused any impairment in channel activity, the SPQ assay was performed for a subset of the Cys mutants (mBBr-labeled) that were predicted to be facing the hydrophobic core according to the crystal structure, which includes R409C, I412C, F413C, L416C, V419C, Y421C, W424C, L428C, F431C, L435C, I437C, V441C, and G444C. The channel activity of these labeled mutants ranged from 72 to 122% of the WT activity level (data not shown). Therefore, attachment of bimane to the Cys residues did not significantly impair the channel activity of the mutant proteins.

Solution Bimane Fluorescence Emission Maxima of Helix 4 and 5 Cys Mutants. The objective of the bimane $\lambda_{em,max}$ measurement is to determine the relative environment of each residue as reported by the bimane fluorophore. Theoretically, more deeply buried residues are expected to have a lower bimane $\lambda_{em,max}$ than solvent-exposed residues in the membrane-bound state. To calibrate the bimane $\lambda_{em,max}$ values, a standard polarity curve was generated previously in our laboratory (*24*) using a bimane-*N*-acetyl-Cys model compound in a series of dioxane/water mixtures with known dielectric constant (ε) values. Previously determined parameters ($\lambda_{em,max}$ < 455 nm = buried; 455 nm < $\lambda_{em,max}$ < 470 nm = moderately accessible; $\lambda_{em,max}$ > 470 nm = solvent-accessible) were applied in this study. Bimane $\lambda_{em,max}$ data shown in panels B and C of Figure 2 suggest that both helices 4 and 5 are amphipathic α-helices that are moderately exposed to the solvent.

Hydrophilic residues based on the crystal structure exhibited bimane $\lambda_{em,max}$ values higher than those of the corresponding hydrophobic residues (Figure 2B,C). Both the crystal structure and bimane $\lambda_{em,max}$ data correlate well with each other and suggested that helix 4 (Lys-406−Leu-416) is a three-cycle α-helix, whereas helix 5 (Lys-420−Tyr-434) is a four-cycle α-helix (Figure 2B,C). Furthermore, data obtained from the solvent-accessible surface areas (SASA) shown in Figure 2A (see Experimental Procedures) also correlate with the bimane $\lambda_{em,max}$ data shown in Figure 2B,C. The similar nature of the data for the soluble and lipid-bound states suggests that both helices 4 and 5 retain their helical patterns in the lipid-bound state. Although it appeared that the helical region of the bimane $\lambda_{em,max}$ data hardly changes upon membrane binding, it is clear that the helix 5 loop region (Leu-435−Asp-446) deviates significantly between the two states even in the absence of H440C data. This is

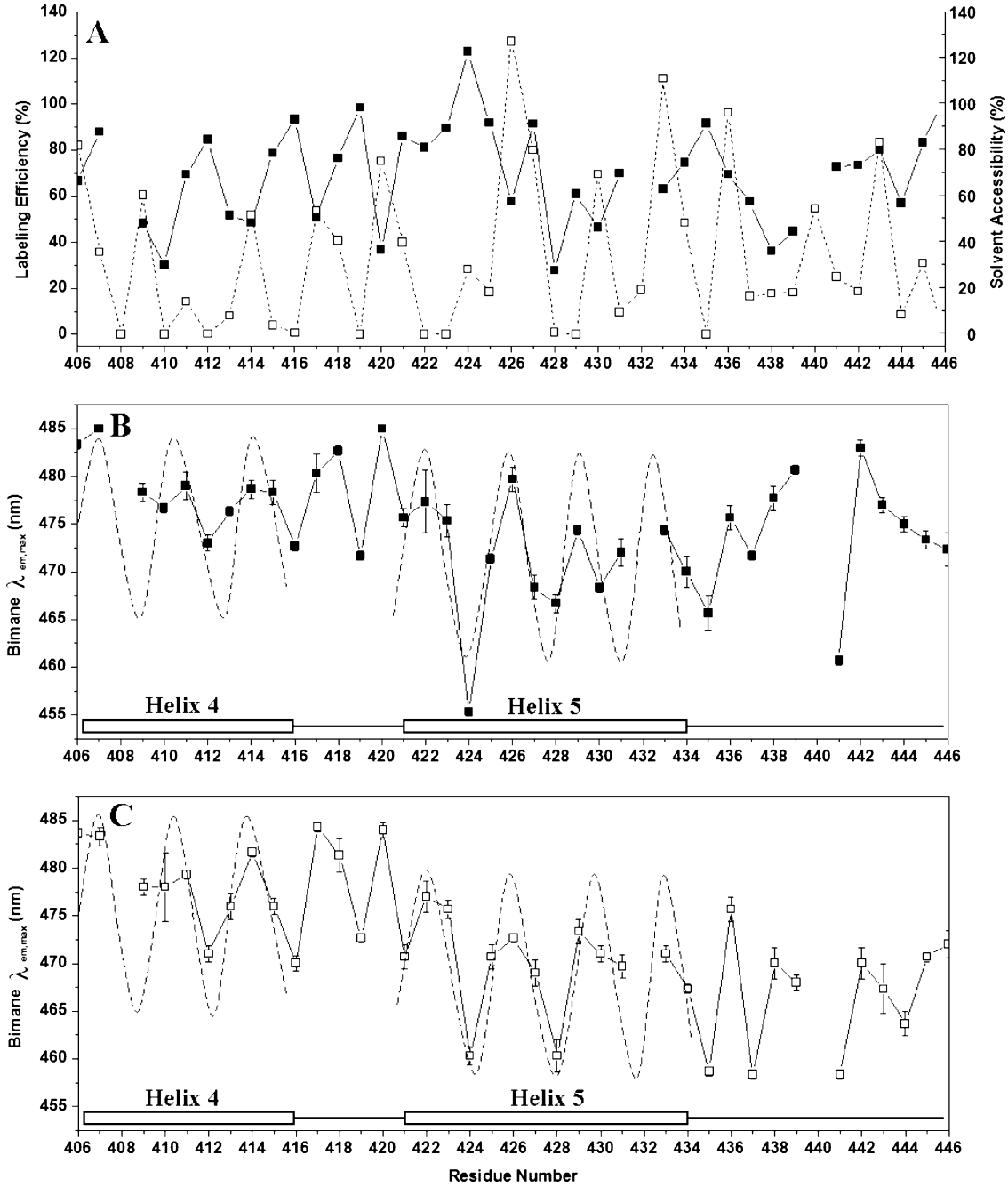

FIGURE 2: Fluorescence emission maximum ($\lambda_{em,max}$) of bimane-labeled Cys mutants of the colicin E1 channel domain and corresponding solvent accessibility vs labeling efficiency of Cys mutants of helices 4 and 5 of the channel peptide. (A) Labeling efficiency (■) and corresponding side chain solvent accessibility (□) of the bimane-labeled cysteine residues. The side chain solvent accessibility (SA) was calculated from the coordinates of the crystal structure of the soluble $P190H_6$ peptide using a 1.4 Å probe as described in Experimental Procedures (PDB entry 2i88). (B) Bimane $\lambda_{em,max}$ values of the Cys mutants in the soluble state (■). (C) Bimane $\lambda_{em,max}$ values of the Cys mutants in the membrane-bound state (□). Data for the two helical regions (helices 4 and 5) were compared against a sine wave function (---) and are represented by rectangles, whereas data for the loop regions are represented by a line. Missing data for certain residues are due to low expression levels of the corresponding mutant proteins. Average values and standard deviations of the bimane $\lambda_{em,max}$ values from at least triplicate measurements are shown.

clearly reflected by the significant changes in the side chains' environment, and this could potentially be due to a major structural rearrangement upon lipid association.

Bimane Fluorescence Anisotropy and Probe Mobility of Helix 4 and 5 Cys Mutants. The probe mobilities of helices 4 and 5 residues were determined from the inverse values of the fluorescence anisotropy measurements in the presence and absence of LUVs. Ideally, surface-exposed residues are expected to have lower anisotropy (higher probe mobility) values given the higher degree of rotational freedom of their side chains. Similarly, buried residues that are facing the interior are expected to have higher anisotropy (lower probe mobility) values. As shown in Figure 3, most Cys mutants have lower probe mobility ($1/r$) values in the membrane-bound state, and this supports the idea that the side chain mobility is usually reduced upon lipid association probably due to steric hindrance.

On the basis of the probe mobility data (Figure 3), there is no doubt that the overall probe mobility of helix 4 is higher than that of helix 5. Interestingly, the probe mobility values

Table 1: Summary of the Fluorescence Measurements of Unlabeled or Labeled Wild-Type and Helix 4 and 5 Cys Mutants of the Colicin E1 Channel Domain

	Trp $\lambda_{em,max}$ (nm)[a]		relative activity (%)[b]
	unlabeled	labeled	unlabeled
WT	324.0 ± 0.0		100 ± 2
K406C	327.3 ± 0.9	328.7 ± 0.9	110 ± 1
A407C	324.0 ± 0.0	323.0 ± 0.8	125 ± 0
D408C	—	—	—
R409C	325.0 ± 0.0	324.7 ± 0.5	121 ± 0
D410C	328.3 ± 0.5	326.7 ± 1.9	84 ± 3
A411C	324.3 ± 0.5	325.3 ± 1.7	117 ± 0
I412C	323.3 ± 0.5	321.0 ± 0.0	106 ± 0
F413C	330.3 ± 0.5	334.7 ± 0.9	88 ± 2
N414C	323.7 ± 0.5	324.3 ± 0.5	99 ± 0
A415C	324.0 ± 0.0	325.7 ± 1.3	111 ± 1
L416C	325.0 ± 0.8	329.3 ± 1.3	96 ± 5
A417C	323.3 ± 0.9	326.3 ± 0.5	86 ± 9
S418C	324.3 ± 0.5	322.0 ± 1.4	99 ± 1
V419C	324.7 ± 0.5	327.3 ± 0.5	110 ± 0
K420C	323.3 ± 0.5	325.0 ± 0.8	99 ± 5
Y421C	326.7 ± 0.5	326.3 ± 0.9	98 ± 4
D422C	323.7 ± 0.9	324.0 ± 0.8	103 ± 9
D423C	327.7 ± 0.5	325.0 ± 1.4	108 ± 3
W424C	324.3 ± 1.3	322.3 ± 0.5	121 ± 2
A425C	324.3 ± 0.5	322.7 ± 1.3	108 ± 3
K426C	322.7 ± 0.9	322.3 ± 2.1	106 ± 5
H427C	329.7 ± 0.5	328.3 ± 0.9	115 ± 5
L428C	323.7 ± 0.5	323.7 ± 0.5	106 ± 1
D429C	326.0 ± 0.8	324.0 ± 0.8	106 ± 3
Q430C	323.7 ± 0.5	323.3 ± 1.3	97 ± 6
F431C	330.0 ± 0.0	331.3 ± 0.5	112 ± 1
A432C	—	—	—
K433C	325.3 ± 0.9	324.3 ± 0.5	92 ± 4
Y434C	328.7 ± 0.5	325.7 ± 0.9	98 ± 2
L435C	324.3 ± 0.5	323.3 ± 0.5	97 ± 4
K436C	323.3 ± 0.5	322.0 ± 0.8	84 ± 4
I437C	326.0 ± 0.8	323.0 ± 0.8	98 ± 6
T438C	326.3 ± 0.9	324.3 ± 0.5	118 ± 0
G439C	325.3 ± 0.9	323.3 ± 0.9	112 ± 4
H440C	—	—	—
V441C	324.0 ± 0.0	322.7 ± 1.7	109 ± 1
S442C	324.0 ± 0.0	323.7 ± 0.9	102 ± 7
F443C	323.7 ± 0.5	323.7 ± 0.5	101 ± 1
G444C	326.7 ± 0.9	323.0 ± 0.8	91 ± 1
Y445C	329.7 ± 0.5	328.0 ± 0.0	101 ± 3
D446C	330.3 ± 0.9	331.3 ± 0.9	98 ± 4

[a] Values shown are means ± the standard deviation for at least triplicate measurements. [b] A channel activity of 100% represents the WT P190H pore forming ability that can release 70% of the Cl^- from the asolectin LUVs. WT channel activity was 3×10^4 Cl^- ions per channel per second.

of both the helix 4 loop region (Ala-417−Lys-420) and the helix 5 loop region (Leu-435−Asp-446) are relatively high probably due to the high flexibility of the loop regions. However, no significant differences were observed between the soluble and lipid-bound states for both loop regions, which suggested that these loops retain their flexibility upon lipid association. Although significant reduction of probe mobility was observed for residue K420 upon membrane association, this can be rationalized on the basis of the high Q-ratio that was observed for K420 (Figure 4B), which reflects the degree of membrane bilayer penetration. In contrast, the probe mobility data clearly contradict the bimane $\lambda_{em,max}$ data, which argue that the helix 5 loop region is more buried in its membrane-bound state. In general, the overall probe mobility data provide strong support for the crystal structure and the bimane $\lambda_{em,\ max}$ data as they all share the same α-helical pattern for both helices 4 and 5.

Dual Quenching Analysis of the Membrane-Bound Depth of Helix 4 and 5 Cys Mutants. To determine the relative membrane penetration depth of helices 4 and 5 in their lipid-bound state, a dual fluorescence quenching method was used (*35*). Two types of quencher species were used in this assay (KI, aqueous quencher; 10-DN, membrane-embedded quencher). Theoretically, surface-exposed residues in the lipid-bound state are expected to be more quenched by KI, resulting in higher values of $F_0/F_{KI} - 1$, where F_0 and F_{KI} represent the fluorescence intensity of bimane in the absence and presence of KI, respectively. In contrast, residues that are buried in the lipid-bound state are expected to be more quenched by 10-DN, resulting in higher values of $F_0/F_{10\text{-}DN} - 1$, as shown in Figure 4B.

Finally, to determine the relative membrane penetration depth, the quenching ratio [Q-ratio; $(F_0/F_{10\text{-}DN} - 1)/(F_0/F_{KI} - 1)$] was calculated. Figure 4B shows the final Q-ratio values for both helices 4 and 5 residues. The Q-ratio data suggested that helix 4 (K406−L416) adopts a tilted topology in its lipid-bound state with its C-terminus more deeply buried than its N-terminus. Although the topology of helix 4 appears to rely on a comparison of only residues 407 and 416 with the exclusion of N414C data, however, it should be noted that the Q-ratios of both S418C and K420C are significantly high. Therefore, it is unlikely that the loop region joining helices 4 and 5, which consists of only four residues, would form a U-shaped loop that shows deep penetration within the membrane bilayer. Although the Q-ratio values of the residues adjacent to N414C are somewhat lower, it does not necessarily reflect the accuracy of the N414C measurement. It should be noted that residue F413 was shown to be a highly pH sensitive residue (*29*); therefore, both mutation and fluorophore attachment at residue F413 may cause significant perturbation that could be reflected in the Q-ratio measurement. In contrast, helix 5 (Tyr-421−Tyr-434) adopts a rather superficial location on the membrane surface with the exception of residue 429 that was measured to be highly quenched by KI (Figure 4A); however, the final calculated Q-ratio for residue 429 appeared to correspond favorably with those of its neighboring residues (Figure 4B). Interestingly, the helix 5 loop region (L435−D446) was shown to be relatively buried within the bilayer (high Q-ratio). Figure 6 illustrates both the predicted two- and three-dimensional models of the lipid-bound state of helices 4 and 5 according to the dual quenching analysis.

Secondary Structure Analysis of Helices 4 and 5. It is clear from the various fluorescence data that both helices 4 and 5 are amphipathic α-helices in both the soluble and membrane-bound states. In fact, it has been determined that an ideal amphipathic α-helix adopts a periodicity range between 3.6 and 3.7 residues per turn (rpt) (*33*). To determine the secondary structure of both helices 4 and 5 of the membrane-bound channel domain, the method developed by Cornette *et al.* (*33*) was used to calculate the periodicity of a given helical sequence on the basis of the fluorescence parameters. To provide a more rigorous analysis, we used Statistical Analysis System (SAS) version 9.1 (see Experimental Procedures), and the various fluorescence parameters were analyzed using a method that we call helix periodicity statistical analysis (HPSA). The process of the analysis basically involves fitting the various fluorescence parameters to eq 3 using four different nonlinear least-squares regression

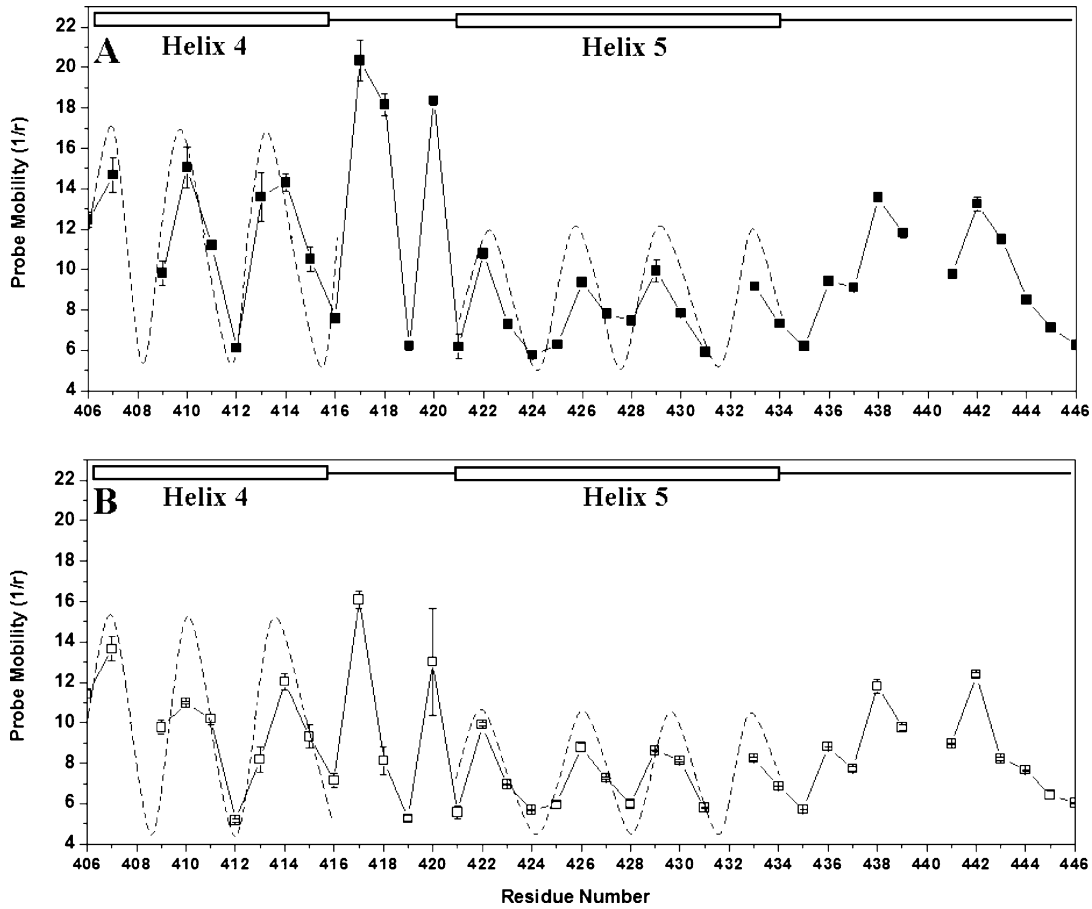

FIGURE 3: Probe mobility of the bimane-labeled Cys mutants of the colicin E1 channel domain. (A) Probe mobility ($1/r$) is calculated as the inverse of the observed fluorescence anisotropy (r). Probe mobility of the bimane-labeled Cys mutants in the soluble state (■). (B) Probe mobility of the bimane-labeled Cys mutants in the membrane-associated state (□). Data for the two helical regions (helices 4 and 5) were compared against a sine wave function (---) and are represented by rectangles, whereas data for the loop regions are represented by a line. Average values and standard deviations for at least triplicate measurements are shown.

analysis methods from the SAS program (gradient, Gauss−Newton, Marquardt, and Newton) to compute the values of a, b, c, and p.

The data listed in Table 2 give a summary of the nonlinear least-squares harmonic wave function analysis of the measured fluorescence parameters of helices 4 and 5 for both the soluble and membrane-bound states. To accurately determine the periodicity and helical boundary of helices 4 and 5, the data collected from dual quenching analysis were not applied in the analysis. The reason behind this approach was due to the Trp quenching effects upon the bimane fluorophore which would theoretically skew the bimane fluorescence intensity. However, both the bimane $\lambda_{em,max}$ and probe mobility ($1/r$) measurements would not be expected to be affected by these quenching effects. It is clear from the analysis that the bimane $\lambda_{em,max}$ and probe mobility ($1/r$) data for both helices 4 and 5 ranged between 3.4 and 4.0, with a standard error (SE) of only 0.1−0.2 in both the soluble and membrane-bound states. Prior to determining the periodicity of helices 4 and 5 using the SAS program, we must first define helical boundaries for both the soluble and membrane-bound states. To help define the helical boundaries of these helices in their membrane-bound states, the residual squared plots were generated to compare the deviation between the experimental fluorescence data and the expected harmonic wave function fit for each residue.

The concept behind this residual squared plot is that residues falling outside the helical region would reflect greater deviation from the harmonic wave function fit in comparison to residues that are within the helical region. In addition, the squaring of the deviation of each residue exaggerates the magnitude of the deviation. Figure 5 shows the squared residual plots of helices 4 and 5 in the membrane-bound state for both the bimane $\lambda_{em,max}$ and probe mobility fluorescence parameters. Fluorescence data for residues Asn-401−Ser-405 were obtained from previously published data (*25*) in identifying the N-terminus of helix 4. Since the fitting program that was used for generating residual squared plots cannot tolerate missing data points, the bimane $\lambda_{em,max}$ and probe mobility data for D408C, A432C, and H440C were simply estimated and entered into the program. It was determined that small changes in these three points did not significantly skew either the calculated periodicities or the helical boundaries. On the basis of the derived residual squared difference plots, it was concluded that the boundaries of helices 4 and 5 in the membrane-bound state range from residue Phe-404 to Ile-437 since residues beyond Lys-403 and Thr-438 appeared to have significantly higher residual squared differences (Figure 5).

To confirm the helical boundary prediction, the Fourier-transform power spectrum analysis was performed for both helices 4 and 5 on the basis of the bimane $\lambda_{em,max}$ and probe mobility fluorescence parameters (Figure 5). It is expected

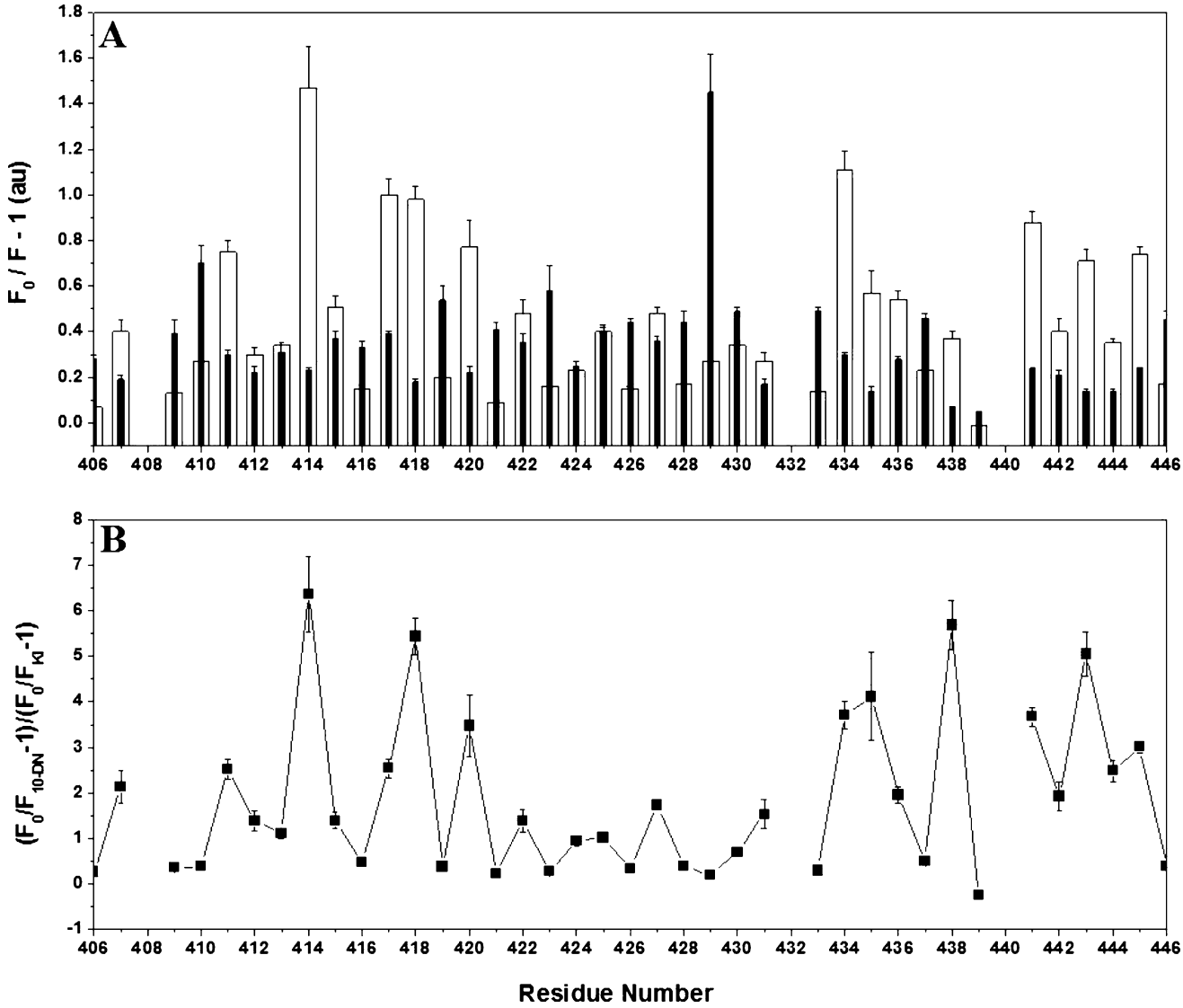

FIGURE 4: Relative membrane bilayer depth for bimane-labeled helix 4 and 5 single-Cys mutant peptides incorporated into lipid vesicles. (A) Histogram showing the bimane fluorescence quenching by KI (black bars) and by 10-DN (white bars). F_0 represents the bimane fluorescence intensity in the absence of quencher(s), whereas F_{KI} and $F_{10\text{-}DN}$ represent the bimane fluorescence intensities in the presence of KI and 10-DN, respectively. (B) Plot of the quenching ratio $[(F_0/F_{10\text{-}DN} - 1)/(F_0/F_{KI} - 1]$ (Q-ratios) for bimane-labeled Cys mutants within helices 4 and 5. The Q-ratio represents the ratio of quenching by 10-DN to that by KI, and it correlates to the penetration depth of the residues within the bilayer; i.e., a higher Q-ratio means that the residue is more deeply buried. Average values and standard deviations from triplicate measurements are shown.

that data with near ideal periodicity for an amphipathic α-helix would produce a single distinct peak at a frequency that corresponds to the periodicity of the given residue sequence. Data shown in Figure 5 (panels I and II) clearly show a distinct peak for both the bimane fluorescence and probe mobility data with a frequency range from 93° to 107° which equals 3.4−3.9 rpt.

Remarkably, the frequency from the power spectrum analysis correlated with the periodicity calculated using the HPSA method from the SAS program. Therefore, the final helical boundary was determined by taking the average of the bimane $\lambda_{em,max}$ values and probe mobility data as shown in Figure 5C. On the basis of the final analysis, we concluded that helix 4 is elongated from Lys-406−Leu-416 in its soluble state to Phe-404−Leu-416 in its membrane-bound state with a frequency of 93.5° which corresponds to 3.8 rpt. In contrast, helix 5 is elongated from Tyr-421−Tyr-434 in its soluble state to Tyr-421−Ile-437 in its membrane-bound state with a frequency of 106.5° which corresponds to 3.4 rpt.

DISCUSSION

Helices 1−3 of the colicin E1 channel domain were previously demonstrated to remain as amphipathic α-helices upon membrane association. Herein, we scanned the membrane-bound topology of helices 4 and 5, which include the voltage sensor of the channel (*36*). We showed that both helices 4 and 5 are also amphipathic α-helices in the membrane-bound state (Table 2). These results support the hypothesis that the closed channel domain of colicin E1 forms an umbrella-like model in which only helices 8 and 9 (hydrophobic helices) are deeply inserted into the hydrophobic milieu of the membrane in the absence of a membrane potential while the eight remaining helices spread out onto the membrane surface (*22*).

A simple model of the membrane-bound colicin E1 channel domain showing the membrane disposition of the first five N-terminal helices is shown in Figure 6A. This model represents the pre-channel state prior to the imposition

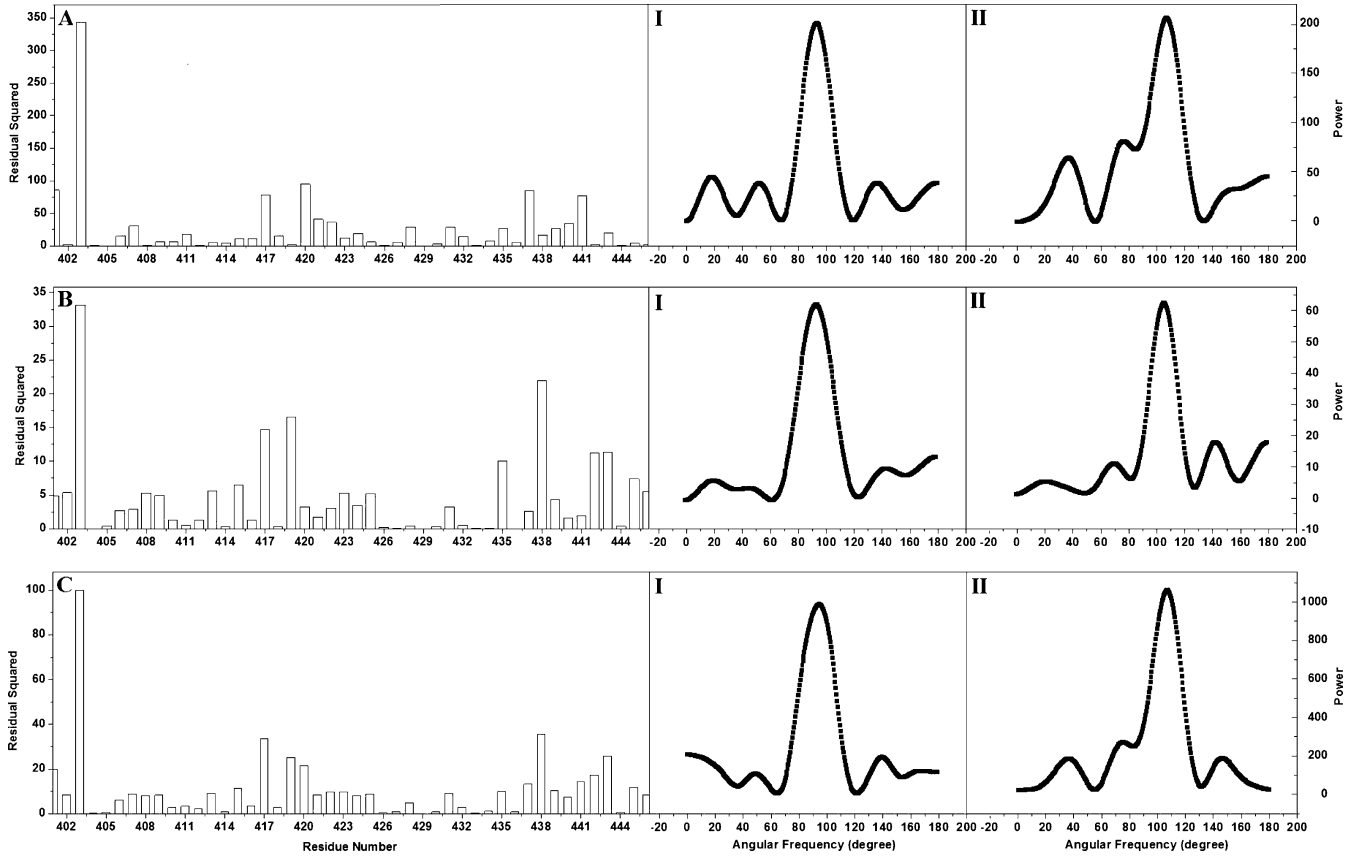

FIGURE 5: Squared residual plot and power spectrum of various fluorescence data for the colicin E1 channel domain in the membrane-associated state. (A) Histogram of the squared residuals for the bimane $\lambda_{em,max}$ data in LUVs. (B) Histogram of the squared residuals of probe mobility ($1/r$) data in LUVs. (C) Histogram of the squared residuals for the average of the bimane $\lambda_{em,max}$ and probe mobility ($1/r$) data in LUVs. The height of the bars indicates the deviation of the fluorescence data from the fit to the harmonic wave function. Panel I represents the Fourier-transform power spectrum of helix 4 in the membrane-bound state, and panel II represents the corresponding spectrum for helix 5. Each power spectrum represents data from the corresponding fluorescence measurement, and the helical segments being analyzed are specified in Table 2. The method of computing the Fourier-transform power spectrum is described in ref *33*.

Table 2: Summary of the Secondary Structure Analysis of the Segment of Lys-401−Asp-446 of the Colicin E1 Channel Domain by HPSA

fluorescence parameter	parameter estimates from HPSA							
	a^a (SE)	b^a (SE) (deg)	c^a (SE)	p^a (SE) (rpt)	frequency (deg)	methods[b]	helix	residues[c]
bimane $\lambda_{em,max}$ (soluble)	2.5 (1.7)	382.0 (0.0)	447.4 (0.0)	3.9 (0.0)	92.6	N	4	406−416
	4.1 (2.2)	383.2 (0.0)	471.3 (1.5)	4.0 (0.0)	90.0	N	5	421−434
bimane $\lambda_{em,max}$ (membrane)	5.6 (1.1)	335.4 (32.8)	477.0 (0.8)	3.8 (0.2)	94.4	GN	4	404−416
	3.2 (1.8)	383.0 (0.4)	470.0 (1.3)	4.0 (0.0)	90.0	N	5	421−436
$1/r$ (soluble)	4.3 (0.5)	306.8 (16.3)	11.0 (0.4)	3.6 (0.1)	99.6	N	4	406−416
	1.8 (0.4)	265.4 (22.9)	8.0 (0.3)	3.4 (0.1)	105.4	GN	5	421−436
$1/r$ (membrane)	3.2 (0.7)	336.3 (32.4)	9.3 (0.5)	3.8 (0.2)	95.6	N	4	404−416
	0.8 (0.4)	383.1 (0.4)	7.2 (0.4)	4.0 (0.1)	90.0	N	5	421−437

[a] The *a*, *b*, *c*, and *p* parameters refer to those used in eq 3. SE is the estimated standard error of each parameter. [b] The four methods of nonlinear least-squares fit used in the HPSA analysis are gradient (G), Gauss−Newton (GN), Marquardt (M), and Newton (N). [c] The sequence ranges of the residues that were included in the HPSA fitting analysis.

of a membrane potential, which would be expected to drive the amphipathic α-helices into the membrane in a parallel orientation (*36*). On the basis of the result of both the harmonic wave function analysis and the dual quenching bilayer depth measurement, a two-dimensional membrane-bound structure of helices 4 and 5 was constructed (Figure 6B). Helix 4 appears to be tightly appressed to the bilayer surface with its C-terminus considerably more buried than its N-terminus. However, helix 5 is more loosely associated with the membrane surface and is not as deeply buried as helix 4. Interestingly, the loop region between helices 5 and 6 is relatively buried which teases the speculation of the possibility that helix 6, or possibly its N-terminus, may be deeply embedded within the membrane bilayer.

Upon initial inspection, our data indicate that both helices 4 and 5 are elongated upon membrane association, and this may seem to contradict the previous model in which the pH trigger mechanism involves a helix-to-coil transition in the activation step. However, the earlier observation based on CD analysis of the colicin E1 channel domain showed that the protein experiences an increase in helical content when membrane bound (*37*). Therefore, it is likely that the helix-to-coil transition associated with membrane binding facilitates the insertion of the helix 8 and 9 hydrophobic hairpin into

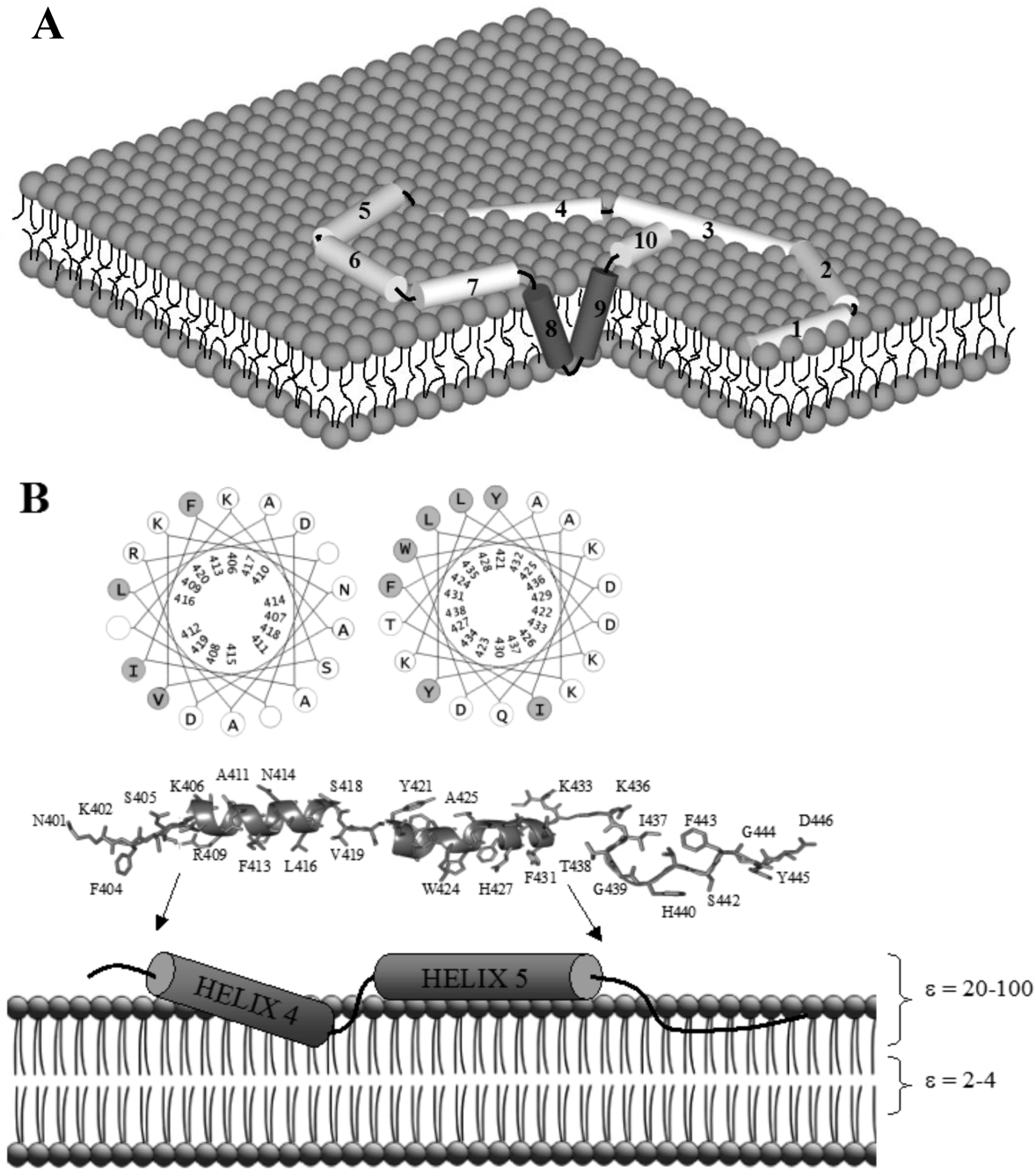

FIGURE 6: Predicted structural model of the membrane-bound topology of the colicin E1 channel domain at zero membrane potential. (A) Low-resolution three-dimensional membrane-bound topology model of the colicin E1 channel domain illustrating the relative depth and position of helices 1−10. Each individual helix is shown as a cylinder with loop regions connecting helices shown as dark lines, and previously measured interhelical FRET distances were also taken into account (*4*). (B) Two-dimensional membrane-bound topology model of helices 4 and 5 of the colicin E1 channel domain. Illustrated in the top panel are the helical wheel projections of helices 4 and 5 with the nonpolar residues shown as gray circles and polar residues as white circles. Shown in the middle panel is the crystal structure of helices 4 and 5 with labeled side chains. Nonpolar residues are facing the membrane toward the bilayer, while polar residues are facing the aqueous side. The bottom panel illustrates the penetration depth, and the helical elongation of helices 4 and 5 is shown as cylinders connected with loop regions shown as dark lines. The penetration depth of each helix relative to the bilayer was calibrated using dielectric constants that were measured from the bimane $\lambda_{em,max}$ data as described previously (*24*).

the membrane bilayer. This transition may be highly dynamic, and upon colicin stabilization at the membrane surface, the helices may evolve into the more extended structures proposed from the data herein. Clearly, our data suggest that only the N-terminus of helix 4 and the C-terminus of helix 5 are elongated upon membrane association (Figure 5). In contrast, Salwinski and Hubbell *et al.* (*27*) conducted an EPR study on the membrane-bound topology of helix 4 that overlapped with the N-terminal portion of helix 5 (Lys-402−Trp-424). It was proposed that helix 4 is elongated upon membrane association from Lys-406−Leu-416 to Lys-402−Lys-420, and this clearly contradicts our results in this work. If, however, the C-terminus of helix 4 is elongated from Leu-416 to Lys-420, then both helices 4 and 5 must combine to form one giant helix upon membrane association. However, the squared residual plot results (Figure 5) based on all the fluorescence parameters clearly demonstrate that there is little, if any, helical structure

in the Ala-417−Lys-420 segment, which strongly argues that helices 4 and 5 of the channel domain remain separate in the membrane-bound state. In addition, both the bimane $\lambda_{em,max}$ and probe mobility data strongly suggest that the periodicity of the loop region connecting helices 4 and 5 is simply out of phrase with the helical context of the channel domain and must therefore be non-helical.

Although the precise helical boundary differences for helices 4 and 5 between this study and the previous EPR investigation could be ascribed to differences in both the lipid composition and pH in the experiments, it should also be noted that both EPR and fluorescence report on different physical properties of the helices. In fact, both the probe mobility and the membrane penetration depth correlate well with one another for the two studies. Spin-labeled Cys residues that showed reduced probe mobility from the EPR study also had a corresponding lower probe mobility in our study (Figure 3) and vice versa (*27*). In addition, both the EPR data and our dual quenching analysis indicate that helix 4 adopts a tilted topology with its C-terminus relatively deeply buried within the bilayer membrane (*27*). It has been proposed that tilted helical peptides are an important structural motif involved in membrane protein insertion for viral and bacterial proteins (*38*). Furthermore, hydrophobic residues on the nonpolar face of this helix as seen in the crystal structure also exhibited lower solvent accessibility in both studies. Although it was suggested from the EPR study that helices 4 and 5 might be aligned perpendicular to the membrane, it is clear from our data that both helices are amphipathic in nature. Therefore, the likelihood for these structures to adopt a transmembrane configuration in isolation is quite remote. In addition, the EPR study did not pursue measurements past residue W424, and this simply does not provide sufficient data for the prediction of the entire helix 5 topology.

In relation to a previous study from our laboratory on the investigation of the pH sensitive region of the colicin E1 channel domain (*30*), it was interesting to note that many of the solubility issues involving helix 4 single-Cys mutant proteins involved sites that were shown to be pH sensitive residues, including Ser-405, Asp-408, Asp-410, Phe-413, Lys-420, Asp-423, and Trp-424. In addition, many of the aforementioned residues also showed red-shifted bimane $\lambda_{em,max}$ values, indicative of a high degree of solvent exposure for these residues. Not surprisingly, the crystal structure revealed that these residues face the aqueous solvent in the water soluble structure. Therefore, it is possible that these residues may form non-covalent interactions between both the translocation and receptor-binding domains to stabilize the channel domain as a water-soluble protein. However, the crystal structure of whole colicin Ia suggested that helix 4 in this analogous channel-forming protein has no interaction with other domains in the structure (*39*). However, the possibility exists that both the translocation and receptor-binding domains of colicin E1 might help stabilize the channel domain indirectly by recruiting other factors that may interact with helix 4 of the channel domain. If this proposal is correct, we would expect that mutation at those critical sites within helix 4 may significantly affect the solubility of the channel domain. In contrast, expression of the corresponding whole colicin mutants may eliminate the solubility issue.

We concluded that both the bimane $\lambda_{em,max}$ and probe mobility data provided accurate and reliable analyses according to both the Fourier-transform power spectra and HPSA analysis using SAS (Table 2 and Figure 5). Therefore, the periodicity calculation based on the two measurements was calculated to be 3.75 ± 0.1 for helix 4 and 3.70 ± 0.1 for helix 5 in the soluble state. Upon membrane association, the periodicity of helix 4 remains unchanged at 3.80 ± 0.2 whereas the periodicity of helix 5 was increased to 4.0 ± 0.1. Our analysis indicated that no significant changes occur with the transition from the soluble to the membrane-bound state of helices 4 and 5 in terms of their periodicities. Helical wheel diagrams of helices 4 and 5 in Figure 6B also supported the amphipathic nature of these two helices. Data from both the bimane $\lambda_{em,max}$ and probe mobility residual squared plots suggested that helix 4 is elongated from Lys-406−Leu-416 in its soluble state to Phe-404−Leu-416 in its membrane-bound state, whereas helix 5 is elongated from Tyr-421−Tyr-434 in its soluble state to Tyr-421−Ile-437 in its membrane-bound state. Therefore, our data strongly suggest that both helices 4 and 5 remain as two separate helices upon the transition from the soluble to membrane-bound states. Notably, our data refute the earlier model of Hubbell *et al.* that suggested the extension of helices 4 and 5 to form one single giant amphipathic α-helix (*27*).

Although the structure of the open channel state of colicin E1 upon voltage imposition has been controversial, it has been widely accepted that the open channel structure consists of an even number of transmembrane helices having both the N- and C-termini lying on the cis side of the membrane. In addition, strong evidence from fluorescently labeled liposome studies (*19*) suggests that both helices 8 and 9 act as the anchor domain contributing to the toroidal pore of colicin E1. However, previous models have proposed that the formation of the open channel state might involve at least two additional transmembrane helices (*10, 26, 36, 40*−*44*). In support of this model, our current data reveal that the loop region of helix 5 is relatively buried within the bilayer (Figure 4), and this leads us to speculate about the possibility that both helices 6 and 7 adopt a transmembrane orientation in the open channel. Furthermore, the fact that our data show that helices 4 and 5 are elongated upon membrane association further supports the toroidal model for the open state of the colicin E1 channel that was previously proposed by Cramer and co-workers (*10, 43*) which features shorter transmembrane helices.

Future research objectives include the elucidation of the membrane-bound topology of the five remaining helices within the channel domain. In addition, we plan to study the topology of the open channel state in the presence of a membrane potential by studying supported planar bilayers on gold electrodes. Furthermore, we will apply FRET techniques involving Trp donors with Cys-bimane acceptor fluorophores to build a low-resolution three-dimensional structure of the membrane-bound channel by measuring the interhelical distances relative to the three natural Trp residues in a helix-by-helix fashion. These experiments should provide complementary and insightful data regarding the tertiary structure of the membrane-associated channel domain.

ACKNOWLEDGMENT

We thank Zhikui Wei for assistance in the early stages of this research project. We also thank both Gerry Prentice and Dawn White for excellent technical support. Lastly, we express our appreciation to Professor Erwin London (State

University of New York, Stony Brook, NY) for the gift of the 10-DN for use in the Q-ratio measurements.

REFERENCES

1. Pugsley, A. P. (1984) The ins and outs of colicins. Part II. Lethal action, immunity and ecological implications. *Microbiol. Sci. 1*, 203–205.
2. Cooper, P. C., and James, R. (1984) Two new E colicins, E8 and E9, produced by a strain of *Escherichia coli*. *J. Gen. Microbiol. 130*, 209–215.
3. Lazdunski, C. J., Bouveret, E., Rigal, A., Journet, L., Lloubes, R., and Benedetti, H. (1998) Colicin import into *Escherichia coli* cells. *J. Bacteriol. 180*, 4993–5002.
4. Lindeberg, M., Zakharov, S. D., and Cramer, W. A. (2000) Unfolding pathway of the colicin E1 channel protein on a membrane surface. *J. Mol. Biol. 295*, 679–692.
5. Berne, S., Sepcic, K., Anderluh, G., Turk, T., Macek, P., and Poklar, U. N. (2005) Effect of pH on the pore forming activity and conformational stability of ostreolysin, a lipid raft-binding protein from the edible mushroom *Pleurotus ostreatus*. *Biochemistry 44*, 11137–11147.
6. Ladokhin, A. S., Isas, J. M., Haigler, H. T., and White, S. H. (2002) Determining the membrane topology of proteins: Insertion pathway of a transmembrane helix of annexin 12. *Biochemistry 41*, 13617–13626.
7. Garcia-Saez, A. J., Mingarro, I., Perez-Paya, E., and Salgado, J. (2004) Membrane-insertion fragments of Bcl-xL, Bax, and Bid. *Biochemistry 43*, 10930–10943.
8. Schendel, S. L., Montal, M., and Reed, J. C. (1998) Bcl-2 family proteins as ion-channels. *Cell Death Differ. 5*, 372–380.
9. Filloux, A., Voulhoux, R., Ize, B., Gerard, F., Ball, G., and Wu, L. F. (2002) Use of colicin-based genetic tools for studying bacterial protein transport. *Biochimie 84*, 489–497.
10. Zakharov, S. D., Kotova, E. A., Antonenko, Y. N., and Cramer, W. A. (2004) On the role of lipid in colicin pore formation. *Biochim. Biophys. Acta 1666*, 239–249.
11. Elkins, P., Bunker, A., Cramer, W. A., and Stauffacher, C. V. (1997) A mechanism for toxin insertion into membranes is suggested by the crystal structure of the channel-forming domain of colicin E1. *Structure 5*, 443–458.
12. Stroud, R. M., Reiling, K., Wiener, M., and Freymann, D. (1998) Ion-channel-forming colicins. *Curr. Opin. Struct. Biol. 8*, 525–533.
13. Zakharov, S. D., and Cramer, W. A. (2004) On the mechanism and pathway of colicin import across the *E. coli* outer membrane. *Front. Biosci. 9*, 1311–1317.
14. Tian, C., Tetreault, E., Huang, C. K., and Dahms, T. E. (2006) Electrostatic interactions of colicin E1 with the surface of *Escherichia coli* total lipid. *Biochim. Biophys. Acta 1758*, 693–701.
15. Gouaux, E. (1997) The long and short of colicin action: The molecular basis for the biological activity of channel-forming colicins. *Structure 5*, 313–317.
16. Elkins, P. A., Song, H. Y., Cramer, W. A., and Stauffacher, C. V. (1994) Crystallization and characterization of colicin E1 channel-forming polypeptides. *Proteins 19*, 150–157.
17. Parker, M. W., Postma, J. P., Pattus, F., Tucker, A. D., and Tsernoglou, D. (1992) Refined structure of the pore-forming domain of colicin A at 2.4 Å resolution. *J. Mol. Biol. 224*, 639–657.
18. Malenbaum, S. E., Merrill, A. R., and London, E. (1998) Membrane-inserted colicin E1 channel domain: A topological survey by fluorescence quenching suggests that model membrane thickness affects membrane penetration. *J. Nat. Toxins 7*, 269–290.
19. Lins, L., El, K. K., Charloteaux, B., Flore, C., Stroobant, V., Thomas, A., Dufrene, Y., and Brasseur, R. (2007) Lipid-destabilizing properties of the hydrophobic helices H8 and H9 from colicin E1. *Mol. Membr. Biol. 24*, 419–430.
20. Zakharov, S. D., and Cramer, W. A. (2002) Colicin crystal structures: Pathways and mechanisms for colicin insertion into membranes. *Biochim. Biophys. Acta 1565*, 333–346.
21. Slatin, S. L., Qiu, X. Q., Jakes, K. S., and Finkelstein, A. (1994) Identification of a translocated protein segment in a voltage-dependent channel. *Nature 371*, 158–161.
22. Cascales, E., Buchanan, S. K., Duche, D., Kleanthous, C., Lloubes, R., Postle, K., Riley, M., Slatin, S., and Cavard, D. (2007) Colicin biology. *Microbiol. Mol. Biol. Rev. 71*, 158–229.
23. Steer, B. A., and Merrill, A. R. (1994) The colicin E1 insertion-competent state: Detection of structural changes using fluorescence resonance energy transfer. *Biochemistry 33*, 1108–1115.
24. Musse, A. A., Wang, J., Deleon, G. P., Prentice, G. A., London, E., and Merrill, A. R. (2006) Scanning the membrane-bound conformation of helix 1 in the colicin E1 channel domain by site-directed fluorescence labeling. *J. Biol. Chem. 281*, 885–895.
25. Wei, Z., White, D., Wang, J., Musse, A. A., and Merrill, A. R. (2007) Tilted, extended, and lying in wait: The membrane-bound topology of residues Lys-381−Ser-405 of the colicin E1 channel domain. *Biochemistry 46*, 6074–6085.
26. White, D., Musse, A. A., Wang, J., London, E., and Merrill, A. R. (2006) Toward elucidating the membrane topology of helix two of the colicin e1 channel domain. *J. Biol. Chem. 281*, 32375–32384.
27. Salwinski, L., and Hubbell, W. L. (1999) Structure in the channel forming domain of colicin E1 bound to membranes: The 402−424 sequence. *Protein Sci. 8*, 562–572.
28. Tory, M. C., and Merrill, A. R. (2002) Determination of membrane protein topology by red-edge excitation shift analysis: Application to the membrane-bound colicin E1 channel peptide. *Biochim. Biophys. Acta 1564*, 435–448.
29. Schendel, S. L., and Reed, J. C. (2000) Measuring pore formation by Bcl-2 family proteins. *Methods Enzymol. 322*, 274–282.
30. Musse, A. A., and Merrill, A. R. (2003) The molecular basis for the pH-activation mechanism in the channel-forming bacterial colicin E1. *J. Biol. Chem. 278*, 24491–24499.
31. Tory, M. C., and Merrill, A. R. (1999) Adventures in membrane protein topology. A study of the membrane-bound state of colicin E1. *J. Biol. Chem. 274*, 24539–24549.
32. Zhao, G., and London, E. (2005) Behavior of Diphtheria Toxin T Domain Containing Substitutions That Block Normal Membrane Insertion at Pro345 and Leu307: Control of Deep Membrane Insertion and Coupling between Deep Insertion of Hydrophobic Subdomains. *Biochemistry 44*, 4488–4498.
33. Cornette, J. L., Cease, K. B., Margalit, H., Spouge, J. L., Berzofsky, J. A., and DeLisi, C. (1987) Hydrophobicity scales and computational techniques for detecting amphipathic structures in proteins. *J. Mol. Biol. 195*, 659–685.
34. Merrill, A. R., Steer, B. A., Prentice, G. A., Weller, M. J., and Szabo, A. G. (1997) Identification of a chameleon-like pH-sensitive segment within the colicin E1 channel domain that may serve as the pH-activated trigger for membrane bilayer association. *Biochemistry 36*, 6874–6884.
35. Caputo, G. A., and London, E. (2003) Using a Novel Dual Fluorescence Quenching Assay for Measurement of Tryptophan Depth within Lipid Bilayers To Determine Hydrophobic α-Helix Locations within Membranes. *Biochemistry 42*, 3265–3274.
36. Merrill, A. R., and Cramer, W. A. (1990) Identification of a voltage-responsive segment of the potential-gated colicin E1 ion channel. *Biochemistry 29*, 8529–8534.
37. Zakharov, S. D., Lindeberg, M., Griko, Y., Salamon, Z., Tollin, G., Prendergast, F. G., and Cramer, W. A. (1998) Membrane-bound state of the colicin E1 channel domain as an extended two-dimensional helical array. *Proc. Natl. Acad. Sci. U.S.A. 95*, 4282–4287.
38. Lins, L., and Brasseur, R. (2008) Tilted peptides: A structural motif involved in protein membrane insertion? *J. Pept. Sci. 14*, 416–422.
39. Ghosh, P., Mel, S. F., and Stroud, R. M. (1994) The domain structure of the ion channel-forming protein colicin Ia. *Nat. Struct. Biol. 1*, 597–604.
40. Zhang, Y. L., and Cramer, W. A. (1992) Constraints imposed by protease accessibility on the trans-membrane and surface topography of the colicin E1 ion channel. *Protein Sci. 1*, 1666–1676.
41. Abrams, C. K., Jakes, K. S., Finkelstein, A., and Slatin, S. L. (1991) Identification of a translocated gating charge in a voltage-dependent channel. Colicin E1 channels in planar phospholipid bilayer membranes. *J. Gen. Physiol. 98*, 77–93.
42. Slatin, S. L., Duche, D., Kienker, P. K., and Baty, D. (2004) Gating movements of colicin A and colicin Ia are different. *J. Membr. Biol. 202*, 73–83.
43. Sobko, A. A., Kotova, E. A., Antonenko, Y. N., Zakharov, S. D., and Cramer, W. A. (2004) Effect of lipids with different spontaneous curvature on the channel activity of colicin E1: Evidence in favor of a toroidal pore. *FEBS Lett. 576*, 205–210.
44. Sobko, A. A., Kotova, E. A., Antonenko, Y. N., Zakharov, S. D., and Cramer, W. A. (2006) Lipid dependence of the channel properties of a colicin E1-lipid toroidal pore. *J. Biol. Chem. 281*, 14408–14416.

BI801906V